The 25 October 2010 Mentawai tsunami earthquake, from real-time discriminants, finite-fault rupture, and tsunami excitation

Andrew V. Newman,[1] Gavin Hayes,[2,3] Yong Wei,[4,5] and Jaime Convers[1]

Received 14 December 2010; revised 19 January 2011; accepted 28 January 2011; published 5 March 2011.

[1] The moment magnitude 7.8 earthquake that struck offshore the Mentawai islands in western Indonesia on 25 October 2010 created a locally large tsunami that caused more than 400 human causalities. We identify this earthquake as a rare slow-source tsunami earthquake based on: 1) disproportionately large tsunami waves; 2) excessive rupture duration near 125 s; 3) predominantly shallow, near-trench slip determined through finite-fault modeling; and 4) deficiencies in energy-to-moment and energy-to-duration-cubed ratios, the latter in near-real time. We detail the real-time solutions that identified the slow-nature of this event, and evaluate how regional reductions in crustal rigidity along the shallow trench as determined by reduced rupture velocity contributed to increased slip, causing the 5–9 m local tsunami runup and observed transoceanic wave heights observed 1600 km to the southeast. **Citation:** Newman, A. V., G. Hayes, Y. Wei, and J. Convers (2011), The 25 October 2010 Mentawai tsunami earthquake, from real-time discriminants, finite-fault rupture, and tsunami excitation, *Geophys. Res. Lett.*, *38*, L05302, doi:10.1029/2010GL046498.

1. Introduction

[2] While any earthquake that creates a tsunami can be classified as "tsunamigenic", the term "tsunami earthquake", hereafter TsE, is reserved for a special class of events that generate tsunamis much larger than expected for their magnitude [*Kanamori*, 1972]. These earthquakes are relatively rare, the classification having been attributed to less than ten events in the past century or so. TsE are normally identified to have anomalously slow rupture velocities, and are thus inefficient at radiating seismic energy, often making such events only weakly felt by local populations. Growing evidence suggests that TsE rupture slowly because they occur in the shallowest segment of the subduction megathrust [*Polet and Kanamori*, 2000], which may have ~1/10th the rigidity μ of the deeper thrust, causing a reduction in shear velocity V_S and hence the rupture velocity V_R, which is usually ~0.8 V_S [*Bilek and Lay*, 1999].

[3] On 25 October a moment magnitude M_W 7.8 earthquake struck just west of the Mentawai Islands off the west coast of Sumatra (Figure 1), generating a surprisingly large local tsunami which caused more than 400 human causalities. The event ruptured immediately updip of and was possibly triggered by stress changes following the September 2007 M_W 8.5 Sumatran earthquake [*Stein*, 1999]. This area may have last ruptured as part of the 1797 and 1833 M_W 8.6–8.9 events, described by *Natawidjaja et al.* [2006] as having as much as 18 m of megathrust slip to explain the coseismic uplift of local microatolls by 3m. Further north, a segment that ruptured in 1861 was likely comparable in magnitude (M_W ~8.5) to the 2005 M_W 8.6 Nias earthquake that ruptured the same approximate area [*Newcomb and McCann*, 1987; *Briggs et al.*, 2006]. Available high-resolution bathymetry along the trench adjacent to the giant 2004 M_W 9.15 Sumatran earthquake suggests that significant faulting in the region may be due to rupture through the prism toe during the 2004 and previous earthquakes [*Henstock et al.*, 2006]. The large slip estimated in the shallow trench during the 1833 earthquake, and the considerable faulting near the trench toe further north support the hypothesis that the subduction zone off western Indonesia is capable of supporting shallow megathrust slip, the type seen in TsE events. This is supported by a recent study that suggests slow rupture of a magnitude 7.6 earthquake offshore Sumatra in 1907 (~2°N) caused a large local tsunami [*Kanamori et al.*, 2010].

2. Real-Time Detection

[4] Using the set of programs called '*RTerg*' (A. V. Newman and J. A. Convers, A rapid energy-duration discriminant for tsunami earthquakes, submitted to *Geophysical Research Letters*, 2010), we automatically determine earthquake energies and estimated rupture durations in near real-time at Georgia Tech for global earthquakes greater than magnitude 6.5, starting in January 2009 (Newman and Convers, submitted manuscript, 2010). This information is useful for rapidly characterizing strong shaking in large earthquakes and its tsunami potential, and is detailed in Text S1 of the auxiliary material.[1]

[5] In the case of the Mentawai earthquake, because the first iterations used data from stations that did not yet record the termination of rupture, the event duration was underreported (Table 1). The first iteration found T_R = 53 s and M_e = 6.95, considerably smaller than the final reported M_W = 7.8. By iteration two, 8.5 minutes after rupture initi-

[1]School of Earth and Atmospheric Science, Georgia Institute of Technology, Atlanta, Georgia, USA.
[2]National Earthquake Information Center, U.S. Geological Survey, Denver, Colorado, USA.
[3]Synergetics Incorporated, Fort Collins, Colorado, USA.
[4]Center for Tsunami Research, Pacific Marine Environment Laboratory, National Oceanographic and Atmospheric Administration, Seattle, Washington, USA.
[5]Joint Institute for the Study of Atmosphere and Ocean, University of Washington, Seattle, Washington, USA.

0094-8276/11/2010GL046498

[1]Auxiliary materials are available in the HTML. doi:10.1029/2010GL046498.

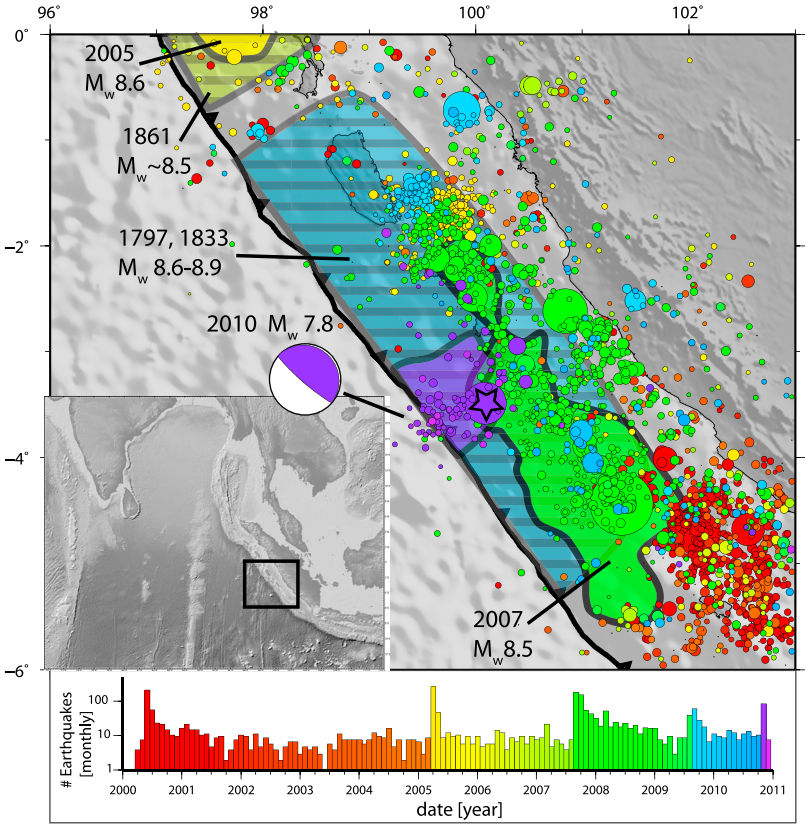

Figure 1. Rupture area of the 2010 Mentawai, and previous historic and recent large earthquakes ([inset] study region highlighted by box). Events include the combined rupture of the 1797 and 1833 M_W 8.6 to 8.9 earthquakes [*Natawidjaja et al.*, 2006], the southern extent of the 1861 and 2005 M_W ~8.6 events [*Newcomb and McCann*, 1987; *Briggs et al.*, 2006], and 2007 M_W 8.5 earthquake [after *Ji et al.*, 2002]. Also shown is the gCMT mechanism and location, and other earthquakes with magnitude >4 since 2000 colored by date and corresponding to histogram. The high-slip area shown in Figure 3 defines the approximate rupture area of the Mentawai event.

ation, T_R increased to 96 s and M_e to 7.17, a result that in retrospect could have identified the event as slow. By the fourth iteration, 16.5 minutes after the rupture began, *RTerg* stabilized to its near final solution with T_R = 126 s and M_e = 7.09. A final determination was made after an analyst reviewed the event, and corrected for the reported global Centroid Moment Tensor (gCMT) focal mechanism [*Ekström et al.*, 2005], finding T_R = 127 s and M_e = 7.03 using 51 stations, comparable but smaller than the final result determined independently by the USGS (M_e = 7.2) [*Choy and Boatwright*, 2007].

[6] While real-time assessments of T_R, and E, are independently useful for assessing the size of a large earthquake, their combination yields a robust discriminant for TsE [*Lomax et al.*, 2007, Newman and Convers, submitted manuscript, 2010]. Because T_R^3 scales with M_0 for most earthquakes [*Houston*, 2001], the long duration of slow-source TsE stand out particularly well when compared to their deficient rupture energy. Newman and Convers (submitted manuscript, 2010) identified that real-time high-frequency solutions are optimal and implemented in *RTerg* a discriminant threshold for TsE to be $E_{hf}/T_R^3 < 5 \times 10^7$ J/s^3. Thus, after iteration 5, the event was automatically classified as a possible TsE, and notifications were sent to a distribution list including individuals from the USGS National Earthquake Information Center (NEIC) and Pacific Tsunami Warning Center (PTWC). The progression of the discriminant in real time is shown along with other post-processed and real time solutions in Figure 2c.

[7] Like other TsE, the 2010 Mentawai earthquake can be uniquely identified as a slow-rupturing TsE through a comparison of its energy to seismic moment M_0 ratio. *Newman and Okal* [1998] initially identified that while most events have $\Theta = \log_{10}(E/M_0)$ between −4.0 and −5.0, slow TsE have $\Theta \leq -5.7$. Using the final energy given the corrected gCMT mechanism, we find the Mentawai earthquake to have $\Theta = -5.9$, clearly discriminating it as a slow-

Table 1. Real-Time and Final Energy and Duration Determinations for 2010 Mentawai Event[a]

Iteration	T_R (s)	E_{hf} ($M_{e\text{-}hf}$) ($\times 10^{14}$ J)	E (M_e) ($\times 10^{14}$ J)	E_{hf}/T_R^3 ($\times 10^7$ J/s^3)	N_{stat}	Latency (s)
1	53	1.3 (6.97)	5.9 (6.95)	85	11	393
2	96	2.2 (7.12)	13.0 (7.17)	24	18	513
3	94	1.0 (6.90)	8.6 (7.06)	12	44	693
4	126	1.0 (6.91)	9.6 (7.09)	5.2	54	993
5	124	0.90 (6.87)	7.6 (7.02)	4.7	51	1615
Final	127	0.91 (6.87)	7.8 (7.03)	4.5	51	N/A

[a]Shown are the high frequency E_{hf} and broadband estimated energies E, their ratio used as the tsunami earthquake discriminant, the number of stations used N_{stat} and the latency of the determination.

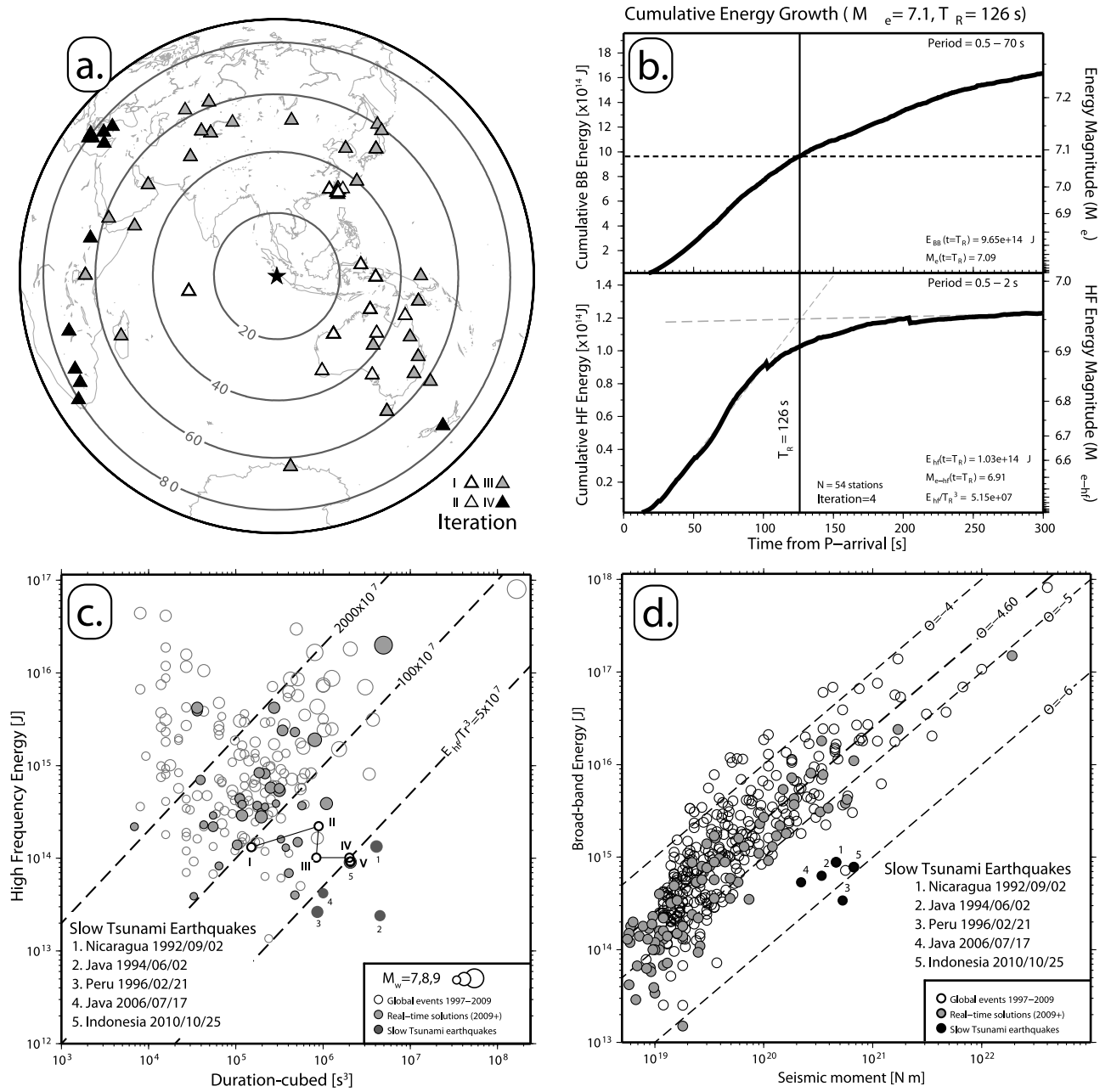

Figure 2. (a) Broadband seismic stations available for real time energy analysis (25°–80°; stations added in subsequent iterations are differentiated by shade). (b) The high-frequency energy growth identifies the approximate event duration T_R while the total event energy E is determined using broadband energy at T_R (iteration 4 shown). (c) The per-iteration (I-V) determination of E/T_R^3 are shown relative to other real-time solutions since 2009 (gray circles), solutions with known mechanisms (open circles), and other TsE events (dark circles). By iteration 4 (IV) the result stabilized and comparable to the final solution determined using the gCMT mechanism (5). (d) Like other TsE, E/M_0 for this event is significantly reduced ($\Theta = -5.9$).

TsE (Figure 2d). Because *RTerg* does not determine focal mechanisms, this solution was not determined in real-time. However, Θ determinations are routine at the PTWC [*Weinstein and Okal*, 2005].

3. Finite-Fault Modeling

[8] Using teleseismic waveforms recorded within the Global Seismic Network, we invert for the source rupture based on the finite fault algorithm of *Ji et al.* [2002], using a 1D velocity model regionally based on Crust2.0 [*Bassin et al.*, 2000] and detailed in Text S1. However, the upper plate in the Mentawai region is reduced in *P*-wave velocity by 30% or more compared to crust landward of the trench and below the fault interface [*Collings et al.*, 2010]. This velocity reduction may be interpreted in global subduction zone environments from teleseismically observed increased T_R corresponding to reduced regional V_R [*Bilek and Lay*,

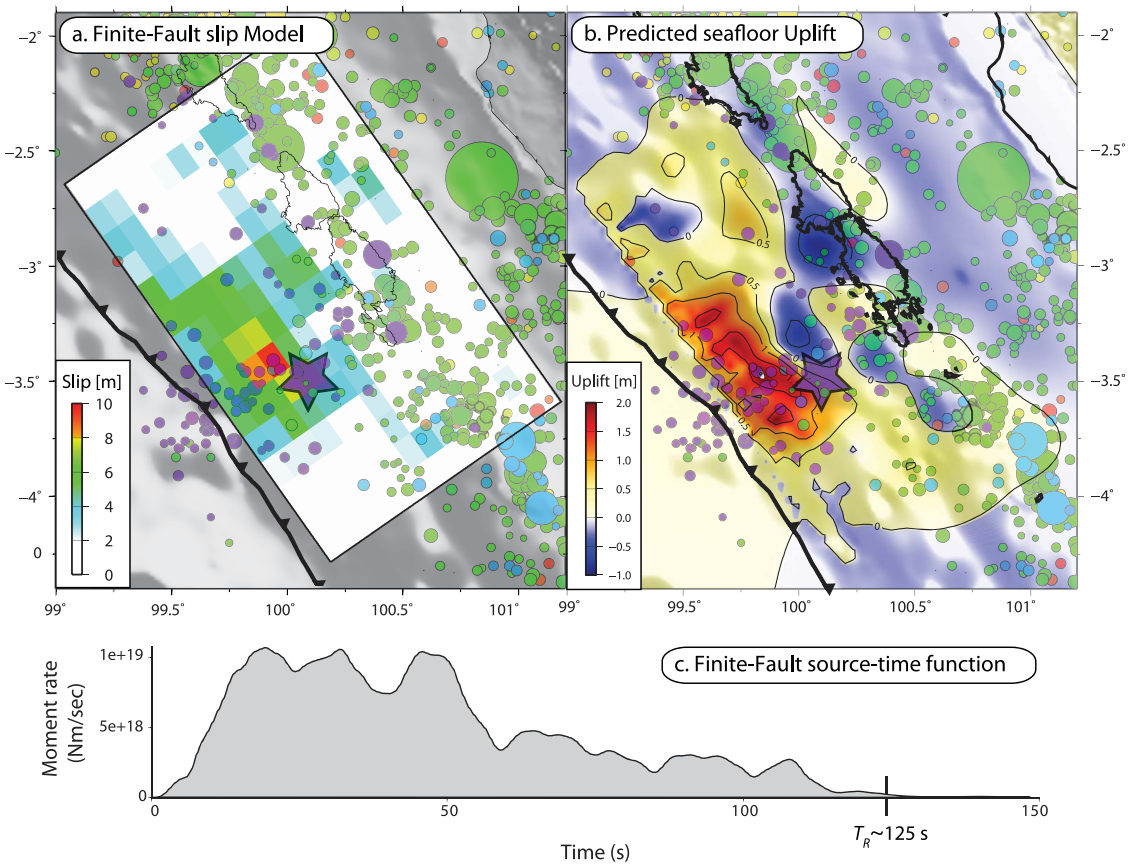

Figure 3. (a) The preferred interface slip model strikes N35°W, and extends from the seafloor to 33.9 km depth at a dip of 11.6°, has primarily thrust motion with large slip focused updip and primarily NE of the hypocenter (star). The spatially distributed slip form the scaled finite fault solution is used as input to predict (b) the surface uplift, and (c) the earthquake source-time function.

1999]. Because tsunami excitation is controlled by the amplitude of upper plate slip and its translation into seafloor uplift, it is necessary to correct for the discrepancy between the teleseismically inverted slip and the true regional slip that may be subdued when traveling through the lower crust. To do so, we variably scale the slip using regional estimates of the shear velocity V_S. To conserve energy that goes into work, M_0 is considered constant, and hence the product of slip $\vec{D}$ and regional rigidity μ are constant assuming constant rupture area:

$$\vec{D}\mu = \vec{D}_0\mu_0.$$

Hence, because V_S^2 is equated to μ divided by density, the scaled fault slip $\vec{D}$ is related to the original finite-fault determined slip $\vec{D}_0$ by the ratio of the squared reference shear velocity used in the inversion $V_{S\text{-}ref}$ and V_s. This can be estimated from V_R, as:

$$\vec{D} = \vec{D}_0\left(\frac{V_{S-ref}}{V_S}\right)^2$$

assuming negligible density changes and $V_S \sim 125\%\ V_R$ [e.g., *Bilek and Lay*, 1999]. The ratio of the squared velocities is the scale-factor χ. Because V_R is spatially variable in the inversion, χ varies across the fault between 3.0 and 8.2 over the sub-fault patches, with a slip-weighted mean = 5.6 ± 1.0. The final scaled model (Figure 3) has a shape similar to the original (Figure S3), but with ~5 times the slip, equating to a new maximum slip of 9.6 m, and yielding a large area of 2+ m uplift (Figure 3b), contributing significantly to the event's tsunami potential. Because many assumptions are necessary to scale slip in this manner, including the differential excitation of surface and body waves, such method should be considered a first-order approximation.

4. Tsunami Modeling

[9] To model the tsunami waves observed in the eastern Indian Ocean we used the Method of Splitting Tsunamis (MOST) model, which is a suite of integrated numerical codes capable of simulating tsunami generation, transoceanic propagation, and its subsequent inundation in the coastal area as described by *Titov and González* [1997]. Because detailed local bathymetry is unavailable, these models do not necessarily yield highly precise inundation scenarios, but are useful for evaluating the average runup, and the overall shape and timing of the open-ocean tsunami waves. Details of the tsunami model are included in Text S1.

[10] For each source model tested, the spatially distributed slip from the original or scaled finite fault solution is used to predict the surface uplift following the dislocation model of *Okada* [1992]. While the finite-fault method inher-

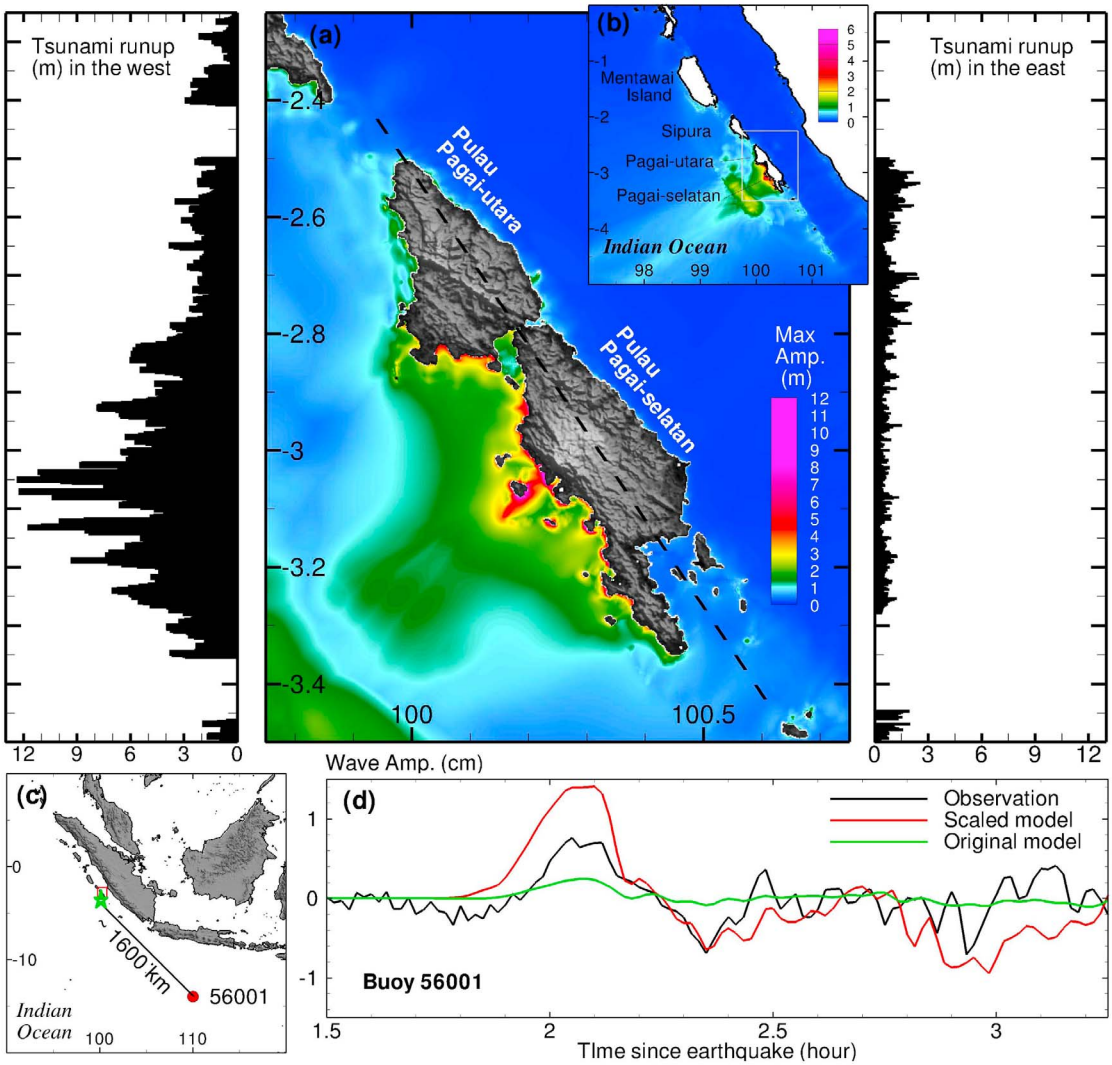

Figure 4. Comparison of tsunami data with model predictions using the seafloor displacement in Figure 3. (a, b) The distribution of predicted (black bars) runup is projected along the E and W sides of the islands (separated by dashed line). (c) An ocean-bottom pressure sensor ~1600 km to the SE (d) observed open-ocean tsunami waves (black line), with timing and period well predicted by the model (red line).

ently solves for the timing of slip along individual patches, the MOST tsunami model requires the seafloor displacement as an instantaneous initial condition, and hence the roughly 125 s rupture duration causes <10% compression of predicted tsunami waves that have a dominant wave period >30 min (Figure 4d).

[11] The preferred scaled source model (Figure 3) leads to promising predicted tsunami results (Figure 4) when compared to preliminary post-tsunami survey results (K. Satake, personal communication, 2010), and deep-ocean observations. The ocean wave height time series recorded by an ocean-bottom pressure sensor ~1,600 km southeast of the earthquake source agrees well with the observed arrival time, wave period, and approximate amplitude (Figures 4c and 4d). While the scaled model overestimates the first wave by about 40%, it more closely represents the observed tsunami than the original unscaled model that under-predicts the observed wave by nearly a factor of 5. While some of the inaccuracy may be due to oceanic bathymetry and detiding effects, it is more likely that the scaled model may still overpredict the maximum slip in the updip region. This likely occurs because the regionally derived variable rigidity along the fault was not used to compute synthetic seismograms, but was inferred from estimated rupture velocities and used to scale slip accordingly. Given the poorly known, three-dimensional velocity structure of the near-source region, the scaling used here is adequate within the framework of uncertainties arising from one-dimensional models commonly used in source inversions. The model predicts a runup distribution along the coastline of the islands, with maximum 3–12 m runup along the western coast and mostly meter-level runup on the eastern coasts (Figure 4a). The western side of the southern Island, Pulau Pagai-seletan, has the highest runup, with sustained values greater than 5–12 m (Figure 4a), comparing well to the range of 5–9 m runup found along the western shore by the Japanese survey team, but overestimates the maximum observed (K. Satake, personal communication, 2010). As previously mentioned, the lack of local high-resolution bathymetry makes more careful direct comparisons unwarranted. An alternative model

developed from a lower-angle finite fault solution (dip = 8° rather than 11.6°) is shown in Figures S4 and S5. This model performs similarly in most aspects, but creates both more variable tsunami runup along the southern island that are not described in initial reports (K. Satake, personal communication, 2010), and more variable coastal subsidence patterns.

5. Discussion

[12] Because TsE are observed in the shallow near-trench region of the subduction interface [*Polet and Kanamori*, 2000], the relatively large distance to the coast, and slowing effect of shallowing ocean on tsunami waves frequently allows for considerable time between the earthquake rupture and tsunami inundation. In the case of the 2006 Java event, the initial positive tsunami waves reached the shore ~40 minutes after the earthquake, and a rapid TsE warning could have been valuable [*Fritz et al.*, 2007]. While, this was not the case for the very proximal Mentawai islands that were likely inundated within 15 minutes of rupture (based on our preferred tsunami model), *RTerg* detected the E_{hf}/T_R^3 discriminant could be useful for most coastal environments. Care should be used in determining an appropriate cut-off value for this discriminant, since an upward shift from the current value of 5 to a more sensitive 25 ($\times 10^7$) J/s^3 would have detected the event as a slow-source TsE as early as 9 minutes after rupture initiation, but with an increased expectation of false-positives (on ~5–10% of events with M ≥ 6.5).

6. Evidence for a Slow-Source Tsunami Earthquake

6.1. Tsunami Size Versus Magnitude

[13] Large regional tsunamis are normally identified for earthquakes $M_W > 8$, however the 2010 Mentawai M_W 7.8 earthquake is reported to have up to 9 m of runup, and an observable cm-level open ocean tsunami 1600 km away. *Kanamori*'s [1972] definition of TsE related the tsunami to higher-frequency body m_b and surface wave M_S magnitudes that are reduced due to slow rupture. This is comparable to the determination of M_e = 7.03, and $M_{e\text{-}hf}$ = 6.87 found in this study, agreeing with m_b = 6.5 and M_S = 7.3 determined by the NEIC; values far too small to otherwise expect an earthquake generated tsunami.

6.2. Long Rupture Duration

[14] Two lines of evidence clearly denote this events' excessive T_R. We identified T_R = 127 s (124 in near-real time) using the termination of continued high-frequency energy growth (Figure 2b). Secondly, as a part of the finite-fault determination, the event source-time function was determined to be nearly identical (~125 s). Such a long duration rupture would scale to an M_W 8.5 earthquake following the relation found by *Houston* [2001].

6.3. Shallow, Near-Trench Rupture

[15] The locations of early aftershocks, the W-phase and gCMT mechanisms, and the area of dominant slip in the finite-fault models, all identify that the event ruptured updip of the point of nucleation (hypocenter) and very near the trench (Figures 1 and 3). Such near-trench rupture is noted as an endemic feature of TsE [*Polet and Kanamori*, 2000], which is likely to control its enhanced tsunami excitation due to increased slip near the free surface [*Satake and Tanioka*, 1999], regardless of the rupture speed (A. V. Newman et al., The energetic 2010 MW 7.1 Solomon Islands Tsunami earthquake, submitted to *Geophysical Journal International*, 2010).

6.4. Deficiency in Radiated Seismic Energy

[16] Using the established E/M_0 [*Newman and Okal*, 1998], and newly tested E_{hf}/T_R^3 discriminants [*Lomax et al.*, 2007, Newman and Convers, submitted manuscript, 2010], we identify this event as a slow rupturing TsE. This event is more deficient than 99.5% of all E/M_0 recorded events since 2000 (J. A. Convers and A. V. Newman, Global evaluation of earthquake energy to moment ratio from 1997 through mid-2010: With improvement for real-time energy estimation, submitted to Journal of Geophysical Research, 2010), and more deficient in E_{hf}/T_R^3 than any other event with $M_e \geq$ 6.5 tested since the beginning of 2008, and similar to the four other slow-source TsE occurred since 1992 (Figure 2d).

7. Conclusions

[17] The M_W 7.8 Mentawai earthquake is a classic example of a rare slow-source tsunami earthquake, exhibiting deficient radiated energy (M_e 7.0) and extended rupture duration (125 s), identifying the characteristically reduced rupture velocity (~1.25–1.5 km/s). Using the spatially determined rupture velocity, we scaled the finite fault derived displacement field to accurately predict the seafloor deformation and observed tsunami excitation. This correction well explains the magnitude and distribution of large 5–9 m local tsunami runup and the timing, wave period and approximate wave heights of the detected transoceanic wave observed 1600 km to the southeast.

[18] **Acknowledgments.** This paper was made possible through the availability of real-time GSN seismic data managed by the USGS-NEIC. We value the constructive reviews by G. Choy, S. Hammond, E. Bernard, S. Weinstein and an anonymous reviewer. USGS-NEHRP grant 08HQGR0028 supported the development of real-time energy calculations.

[19] M. E. Wysession thanks the two anonymous reviewers.

References

Bassin, C., G. Laske, and G. Masters (2000), The current limits of resolution for surface wave tomography in North America, *Eos Trans. AGU*, *81*, F897.

Bilek, S. L., and T. Lay (1999), Rigidity variations with depth along interplate megathrust faults in subduction zones, *Nature*, *400*, 443–446, doi:10.1038/22739.

Briggs, R. W., et al. (2006), Deformation and slip along the Sunda megathrust in the great 2005 Nias-Simeulue earthquake, *Science*, *311*(5769), 1897–2001, doi:10.1126/science.1122602.

Choy, G., and J. Boatwright (2007), The energy radiated by the 26 December 2004 Sumatra-Andaman earthquake estimated from 10-minute *P*-wave windows, *Bull. Seismol. Soc. Am.*, *97*(1A), S18–S24, doi:10.1785/0120050623.

Collings, R., A. Rietbrock, D. Lange, F. Tilmann, D. H. Natawidjaja, B. W. Suwargadi (2010), The structure of the Mentawai segment of the Sumatra subduction zone revealed by local earthquake travel time tomography, *Eos Trans. AGU*, *91*, Fall Meet. Suppl., Abstract T11D-2127.

Ekström, G., A. M. Dziewonski, N. N. Maternovskaya, and M. Nettles (2005), Global seismicity of 2003: Centroid-moment-tensor solutions for 1087 earthquakes, *Phys. Earth Planet. Inter.*, *148*, 327–351, doi:10.1016/j.pepi.2004.09.006.

Fritz, H. M., et al. (2007), Extreme runup from the 17 July 2006 Java tsunami, *Geophys. Res. Lett.*, *34*, L12602, doi:10.1029/2007GL029404.

Henstock, T. J., L. McNeill, and D. Tappin (2006), Seafloor morphology of the Sumatran subduction zone: Surface rupture during megathrust earthquakes?, *Geology*, *34*(6), 485–488, doi:10.1130/22426.1.

Houston, H. (2001), Influence of depth, focal mechanism, and tectonic setting on the shape and duration of earthquake source time functions, *J. Geophys. Res.*, *106*, 11,137–11,150, doi:10.1029/2000JB900468.

Ji, C., D. J. Wald, and D. V. Helmberger (2002), Source description of the 1999 Hector Mine, California earthquake, part I: Wavelet domain inversion theory and resolution analysis, *Bull. Seismol. Soc. Am.*, *92*, 1192–1207, doi:10.1785/0120000916.

Kanamori, H. (1972), Mechanism of tsunami earthquakes, *Phys. Earth Planet. Inter.*, *6*, 346–359, doi:10.1016/0031-9201(72)90058-1.

Kanamori, H., L. Rivera, and W. H. K. Lee (2010), Historical seismograms for unravelling a mysterious earthquake: The 1907 Sumatra earthquake, *Geophys. J. Int.*, *183*, 358–374, doi:10.1111/j.1365-246X.2010.04731.x.

Lomax, A., A. Michelini, and A. Piatanesi (2007), An energy-duration procedure for rapid determination of earthquake magnitude and tsunamigenic potential, *Geophys. J. Int.*, *170*, 1195–1209, doi:10.1111/j.1365-246X.2007.03469.x.

Natawidjaja, D. H., K. Sieh, M. Chlieh, J. Galetzka, B. W. Suwargadi, H. Cheng, R. L. Edwards, J.-P. Avouac, and S. N. Ward (2006), Source parameters of the great Sumatran megathrust earthquakes of 1797 and 1833 inferred from coral microatolls, *J. Geophys. Res.*, *111*, B06403, doi:10.1029/2005JB004025.

Newcomb, K. R., and W. R. McCann (1987), Seismic history and seismotectonics of the Sunda Arc, *J. Geophys. Res.*, *92*, 421–439, doi:10.1029/JB092iB01p00421.

Newman, A. V., and E. A. Okal (1998), Teleseismic estimates of radiated seismic energy: The *E*/*M*0 discriminant for tsunami earthquakes, *J. Geophys. Res.*, *103*, 26,885–26,898, doi:10.1029/98JB02236.

Okada, Y. (1992), Internal deformation due to shear and tensile faults in a half-space, *Bull. Seismol. Soc. Am.*, *82*, 1018–1040.

Polet, J., and H. Kanamori (2000), Shallow subduction zone earthquakes and their tsunamigenic potential, *Geophys. J. Int.*, *142*, 684–702, doi:10.1046/j.1365-246x.2000.00205.x.

Satake, K., and Y. Tanioka (1999), Source of tsunami and tsunamigenic earthquakes in subduction zones, *Pure Appl. Geophys.*, *154*, 467–483, doi:10.1007/s000240050240.

Stein, R. (1999), The role of stress transfer in earthquake occurrence, *Nature*, *402*, 605–609, doi:10.1038/45144.

Titov, V., and F. I. González (1997), Implementation and testing of the Method of Splitting Tsunami (MOST) model, *NOAA Tech. Memo. ERL PMEL-112 (PB98-122773)*, 11 pp., Pac. Mar. Environ. Lab., NOAA, Seattle, Wash.

Weinstein, S., and E. Okal (2005), The mantle wave magnitude M_m and the slowness parameter *THETA*: Five years of real-time use in the context of tsunami warning, *Bull. Seismol. Soc. Am.*, *95*, 779–799, doi:10.1785/0120040112.

J. Convers and A. V. Newman, School of Earth and Atmospheric Science, Georgia Institute of Technology, 311 Ferst Dr., Atlanta, GA 30332, USA. (anewman@gatech.edu)

G. Hayes, National Earthquake Information Center, U.S. Geological Survey, PO Box 25046, MS-966, Denver, CO 80225, USA.

Y. Wei, Center for Tsunami Research, Pacific Marine Environment Laboratory, National Oceanographic and Atmospheric Administration, 7600 Sand Point Way NE, Seattle, WA 98115, USA.

Supplementary Text for: "The 25 October 2010 Mentawai Tsunami Earthquake, from real-time discriminants, finite-fault rupture, and tsunami excitation"

By: Andrew V. Newman, Gavin Hayes, Yong Wei, and Jaime A. Convers

Geophys. Res. Lett., doi:10.1029/2010GL046498, 2011

RTerg Algorithm:

The methodology uses the *P* wave energy in vertical broadband sensors recorded at teleseismic distances from the earthquake following the method of *Boatwright and Choy* [1986], with a correction for real-time focal mechanism [*Newman and Okal,* 1998]. For all recent large earthquakes, once a notification of an event with an initial magnitude ≥5.5 is received from the US Geological Survey's (USGS) Earthquake Information Distribution System (EIDS), *RTerg* queries the USGS's continuous waveform buffer for globally available data and performs per-second calculations of radiated energy growth at each station. The energy is calculated in two distinct bands: broadband energy (0.5 – 70 s period) is used to determine the total earthquake rupture energy E, and high frequency energy E_{hf} (0.5 – 2 s period) used to identify the termination of rupture, and as a discriminant for TsE. Because the first results may run before sufficient data are available at more than a few stations, *RTerg* continues for five iterations, one more than is normally sufficient to capture all available data within the usable teleseismic distances (25° to 80°; **Fig. 2a**).

A unique energy cutoff is determined using the high frequency energy band denoting the approximate end of earthquake rupture. This is currently done using two linear regressions for the constant growth and constant die-off segments of the cumulative energy curves, where the crossover point between regressions approximates the rupture duration T_R (iteration 4 shown in **Fig. 2b**; all iterations and final solution shown in **Fig. S1**). The value of the broadband energy growth at time=T_R, denotes the ultimate E, and energy magnitude, M_e following the conversion by *Choy and Boatwright* [1995]. Additionally, a high frequency energy magnitude $M_{e\text{-}hf}$ can be described using a constant E/E_{hf}=5 [*Newman and Convers,* in revision].

Finite Fault Slip Inversion Method:

We invert for the earthquake rupture model using broadband teleseismic *P* and *SH* body waveforms, and long period surface waves recorded at Global Seismic Network (GSN) stations. After filtering waveforms based on quality (signal-to-noise ratios) and azimuthal distribution, data are converted to displacement using established instrument response information, and then used to constrain the slip history based on the finite fault inversion algorithm of *Ji et al.,* [2002].

Though both nodal planes of the USGS W-Phase solution (*http://neic.usgs.gov*) are tested in the source inversion process, the east-dipping plane, representing the megathrust interface, is preferred based on data fits. For the preferred solution, we adjust the fault geometry to match the geometry of the shallow subduction interface following the technique of *Hayes et al.* [2009].

Rupture velocity V_R is found to be between 0.8-2.5 km/s, constrained by inversion tests starting with constant V_R (optimal V_R = 1.5 km/s). This range is used in all subsequent inversions. The best-fitting (preferred hereafter) inversion recovers ~84% of the teleseismic signal (**Fig. S2**), and finds primarily thrust motion over 100 km fault length, with a maximum slip ~1.8 m and M_0 = 5.7 x 10^{20} Nm (**Fig. S3**). The majority of slip during the earthquake was located west and slightly to the north of the hypocenter (i.e. updip), in agreement with the relative locations of the

hypocenter and W-Phase (and gCMT) centroid solutions, representing the nucleation and average slip locations, respectively (**Fig. S3**). The events' source time function (**Fig. 3c**) indicates fairly rapid build-up and sustained moment release over the first 50 s of slip, before dropping to a lower sustained moment rate out to ~125 s.

Alternative Rupture models:

Similar rupture models are obtained using a range of dips close to our preferred solution, by varying the input data set, and by constraining the rupture velocity to be constant and low ($V_r \leq 2$ km/s), indicating the robustness of the solution.

The MOST Tsunami Modeling algorithms:

The MOST model is a suite of integrated numerical codes capable of simulating tsunami generation, transoceanic propagation, and its subsequent inundation in the coastal area [*Titov and Gonzalez*, 1997]. The MOST propagation uses the non-linear shallow water equation in spherical coordinates with Coriolis force and a numerical dispersion scheme to take into account the different propagation wave speeds with different frequencies. The method of computing inundation is a derivative of the VTCS model that provides finite-difference approximation of the characteristics form of the shallow-water-wave equations using the splitting method [*Titov and Synolakis*, 1995 and 1998]. MOST uses nested computational grids to telescope down into the high-resolution area of interests. Nested grids are used to have a minimum number of nodes in wavelength in order to solve the wave with minimum error. MOST model has been extensively tested against a number of laboratory experiments and benchmarks, and was successfully used for simulations of many historical tsunami events [*Synolakis et al.*, 2008; *Tang et al.*, 2008; *Titov,* 2009; *Wei et al*., 2008]. The MOST model is a standard tsunami inundation model used at NOAA in its tsunami forecast system, known as Short-term Inundation Forecast of Tsunami (SIFT), to provide modeling assistance to Tsunami Warning Centers for their forecasting operations.

Accurate high-resolution bathymetric and topographic data are critical to evaluating tsunami wave dynamics in the costal environment [*Mofjeld et al*., 2001; *Tang et al.*, 2008]. For the ocean wide modeling, a 2' grid, derived from ETOPO1 [*Amante and Eakins*, 2009] is implemented to compute the wave propagation in the Indian Ocean Basin. Due to a lack of high-resolution near-shore bathymetry and coastal topography, the ETOPO1 bathymetry and the Shutter Radar Topography Mission (SRTM) 90 m digital elevation topography are combined and interpolated into three telescoped grids at 30", 15", and 6" to accurately simulate the tsunami impact in the Mentawai region (**Fig. 4b**). The finest 6" grids provide a more realistic model estimation of the waves around Pulau Pagai-selatan, where the catastrophic tsunami impact has been reported [*K. Satake,* 2010, personal communication]. We note that the tsunami runup modeling based on the 6" grid is aimed at developing a preliminary understanding of the tsunami impact along the Mentawai region, and evaluating the quality of earthquake the source model. Because detailed local bathymetry is unavailable, these models are not expected to yield highly precise inundation scenarios for this event, unlike the recent success of modeling the April 1, 2007 Solomon tsunami [*Fritz and Kalligeris,* 2008; *Chen et al.,* 2009; *Wei et al.*, 2010].

Additional References:

Amante, C. and B. W. Eakins (2009). ETOPO1 1 Arc-Minute Global Relief Model: Procedures, Data Sources and Analysis. *NOAA Technical Memorandum NESDIS NGDC-24*, 19 pp.

Boatwright, J. and G. L. Choy (1986). Teleseismic Estimates of the Energy Radiated by Shallow Earthquakes, *J. Geophys. Res.* **91** (B2) p. 2095-2112.

Chen, T., A. V. Newman, L, Feng, H. M. Fritz (2009). Slip Distribution from the 1 April 2007 Solomon Islands Earthquake: A Unique Image of Near-Trench Rupture, *Geophys. Res. Lett.*, 36, L16307, doi:10.1029/2009GL039496.

Fritz, H. & Kalligeris, N., (2008). Ancestral heritage saves tribes during 1 April 2007 Solomon Islands tsunami, *Geophys. Res. Lett.*, 35, L01607, doi: 10.1029/2007GL031654.

Mofjeld, H.O., V.V. Titov, F.I. González, and J.C. Newman (2001). Tsunami scattering provinces in the Pacific Ocean. *Geophys. Res. Lett., 28*(2), 335–337.

Synolakis, C.E., E.N. Bernard, V.V. Titov, U. Kânoğlu, and F.I. González (2008): Validation and verification of tsunami numerical models. *Pure Appl. Geophys.*, *165*(11–12), 2197–2228.

Tang, L., V. V. Titov, and C. D. Chamberlin (2009), Development, testing, and applications of site-specific tsunami inundation models for real-time forecasting, *J. Geophys. Res.*, 114, C12025, doi:10.1029/2009JC005476.

Tang, L., V.V. Titov, Y. Wei, H.O. Mofjeld, M. Spillane, D. Arcas, E.N. Bernard, C. Chamberlin, E. Gica, and J. Newman (2008): Tsunami forecast analysis for the May 2006 Tonga tsunami. *J. Geophys. Res.*, *113*, C12015, doi: 10.1029/2008JC004922.

Titov, V.V. (2009): Tsunami forecasting. Chapter 12 in *The Sea, Volume 15: Tsunamis*, Harvard University Press, Cambridge, MA and London, England, 371–400.

Titov, V.V. and C.E. Synolakis (1995): Modeling of breaking and nonbreaking long wave evolution and runup using VTCS-2. *J. Waterways, Ports, Coastal and Ocean Eng.,* 121(6), 308-316.

Titov, V.V. and Synolakis, C.E. (1998): Numerical modeling of tidal wave runup. *J. Waterway, Ports, Coastal and Ocean Eng.*, 124(4), 157-171.

Wei, Y., E. Bernard, L. Tang, R. Weiss, V. Titov, C. Moore, M. Spillane, M. Hopkins, and U. Kânoğlu (2008): Real-time experimental forecast of the Peruvian tsunami of August 2007 for U.S. coastlines. *Geophys. Res. Lett.*, *35*, L04609, doi: 10.1029/2007GL032250.

Wei, Y., H.M. Fritz, V.V. Titov, B. Uslu, C. Chamberlin, and N. Kalligeris (2010). Solomon Islands 2007 tsunami near-filed modeling and source earthquake deformation, submitted to *Geophys. Journ. Inter.*, in review.

Figure S1: Solutions for earthquake energies (high frequency and broadband) and duration are shown for each of the five real-time iterations and the post-processed result using the gCMT determined focal mechanism (lower right) described in **Table 1.** Early results present artificially shortened T_R because insufficient data had yet arrived at many of the available stations to determine the full rupture duration. Details of individual figures are described in Figure 2b.

Figure S2: Waveform fits for our preferred rupture model, for teleseismic *P*- and *SH*- body waves [a], and long period Rayleigh [b] and Love [c] waves. Data are shown in black, and synthetic fits in red. The number at the end of each trace is the peak amplitude of the observation in micrometers. At the beginning of each trace, the upper number represents the source azimuth, and the lower number the epicentral distance. The shading of each trace describes the relative weighting of the waveforms (lighter shading implies lower weighting).

Figure S3: [a] Cross-section of slip distribution for our alternate rupture model, using a plane better aligned with the shallow geometry of the Sumatra subduction zone, striking 325° and dipping 8° northeast. Colors represent sub-fault slip magnitude; black arrows illustrate slip of the hanging wall relative to the footwall. Contours represent the position of the rupture front with time, plotted and labeled at 5 s and 30 s intervals, respectively. The red star represents the hypocenter of the earthquake. [b] Rupture velocity of our alternate rupture model, contoured at 0.25 km/s intervals. [c] The scaled slip distribution of our alternate rupture model, using the rupture velocity in [b] and following the approach outlined in the main text.

Figure S4: Alterative fault model (similar to **Fig. 3**) with dip=8°. [a] The alternative interface slip model has primarily thrust motion with slip dominated around hypocenter (star). [b] The spatially distributed slip form the finite fault solution in [a] is used as input to predict the surface uplift. [c] Also shown is the earthquake source-time function for this (filled gray curve) and the preferred model (dashed line—**Fig. 3c**).

Figure S5: Alternative tsunami model determined from the finite fault model shown in **Figure S4.** [a,b] The spatial distribution of predicted (black bars) tsunami runup is projected along the eastern and western sides of the islands (separated by dashed black line). [c] An ocean-bottom pressure sensors approximately 1600 km southeast of the event [d] observed cm-level open-ocean tsunami waves (black line). This model performs comparably to the higher-angle dip model in **Figures 3 and 4**, but has more variability in tsunami runup predicted along the western coast of Pulau Pagai-selatan, a result that does not well match the initial reports [*K. Satake,* 2010 personal communication].

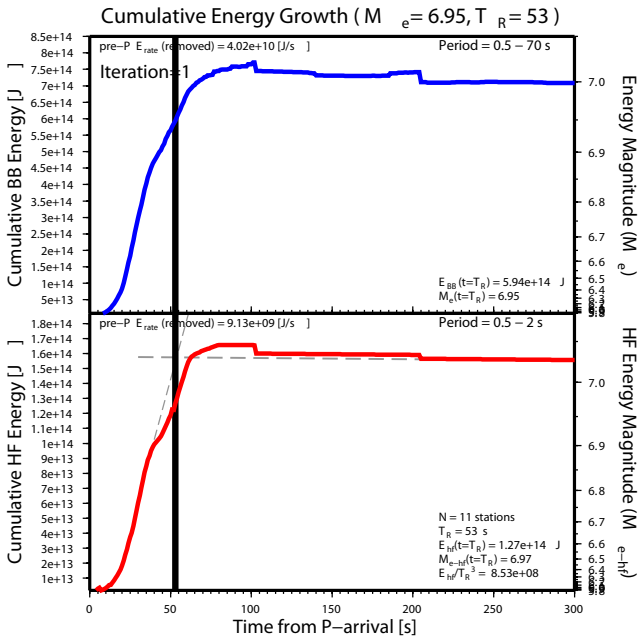
Cumulative Energy Growth (M e= 6.95, T R= 53)
Iteration=1
pre−P E rate (removed) = 4.02e+10 [J/s]
Period = 0.5 − 70 s
E BB (t=T R) = 5.94e+14 J
M e(t=T R) = 6.95
pre−P E rate (removed) = 9.13e+09 [J/s]
Period = 0.5 − 2 s
N = 11 stations
T R = 53 s
E hf(t=T R) = 1.27e+14 J
M e−hf(t=T R) = 6.97
E hf/T R 3 = 8.53e+08
Cumulative BB Energy [J]
Cumulative HF Energy [J]
Energy Magnitude (M e)
HF Energy Magnitude (M e−hf)
Time from P−arrival [s]

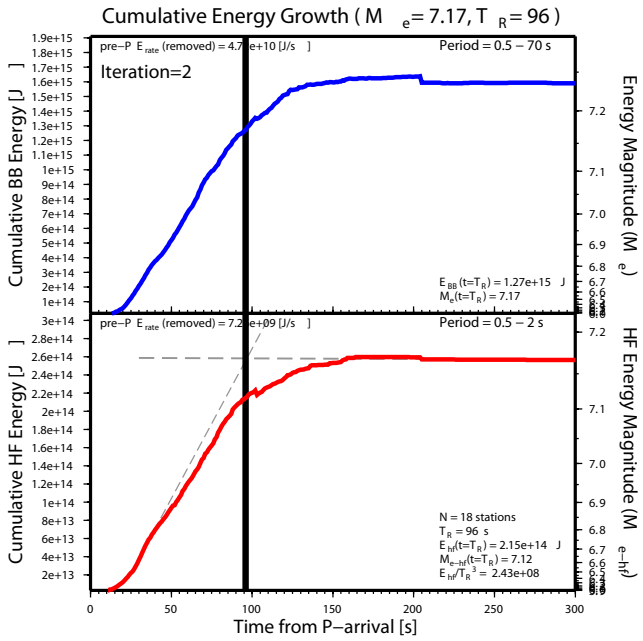
Cumulative Energy Growth (M e= 7.17, T R= 96)
Iteration=2
pre−P E rate (removed) = 4.7 e+10 [J/s]
Period = 0.5 − 70 s
E BB (t=T R) = 1.27e+15 J
M e(t=T R) = 7.17
pre−P E rate (removed) = 7.2 e+09 [J/s]
Period = 0.5 − 2 s
N = 18 stations
T R = 96 s
E hf(t=T R) = 2.15e+14 J
M e−hf(t=T R) = 7.12
E hf/T R 3 = 2.43e+08
Cumulative BB Energy [J]
Cumulative HF Energy [J]
Energy Magnitude (M e)
HF Energy Magnitude (M e−hf)
Time from P−arrival [s]

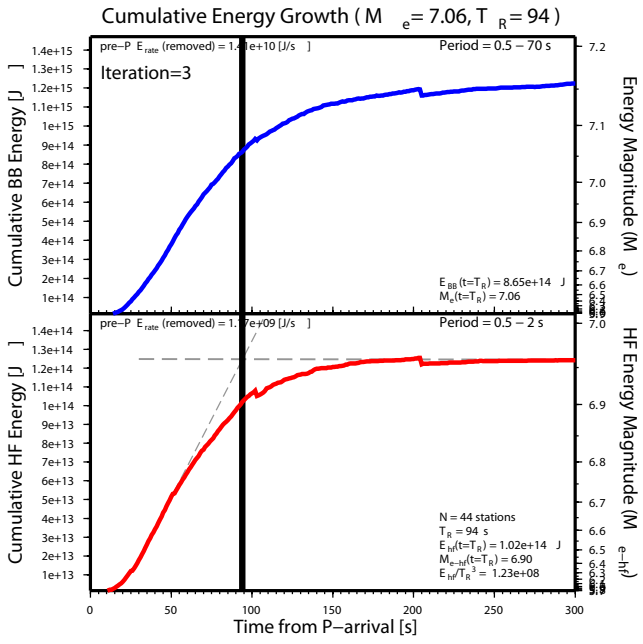
Cumulative Energy Growth (M e= 7.06, T R= 94)
Iteration=3
pre−P E rate (removed) = 1.4 e+10 [J/s]
Period = 0.5 − 70 s
E BB (t=T R) = 8.65e+14 J
M e(t=T R) = 7.06
pre−P E rate (removed) = 1.7 e+09 [J/s]
Period = 0.5 − 2 s
N = 44 stations
T R = 94 s
E hf(t=T R) = 1.02e+14 J
M e−hf(t=T R) = 6.90
E hf/T R 3 = 1.23e+08
Cumulative BB Energy [J]
Cumulative HF Energy [J]
Energy Magnitude (M e)
HF Energy Magnitude (M e−hf)
Time from P−arrival [s]

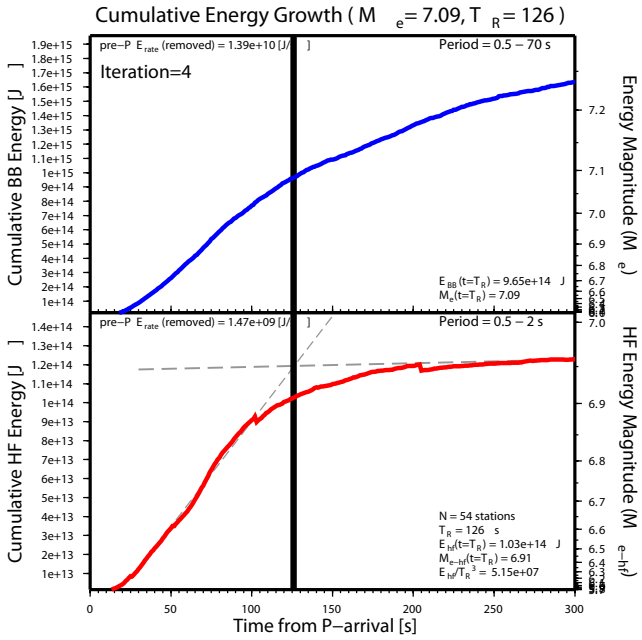
Cumulative Energy Growth (M e= 7.09, T R= 126)
Iteration=4
pre−P E rate (removed) = 1.39e+10 [J/
Period = 0.5 − 70 s
E BB (t=T R) = 9.65e+14 J
M e(t=T R) = 7.09
pre−P E rate (removed) = 1.47e+09 [J/
Period = 0.5 − 2 s
N = 54 stations
T R = 126 s
E hf(t=T R) = 1.03e+14 J
M e−hf(t=T R) = 6.91
E hf/T R 3 = 5.15e+07
Cumulative BB Energy [J]
Cumulative HF Energy [J]
Energy Magnitude (M e)
HF Energy Magnitude (M e−hf)
Time from P−arrival [s]

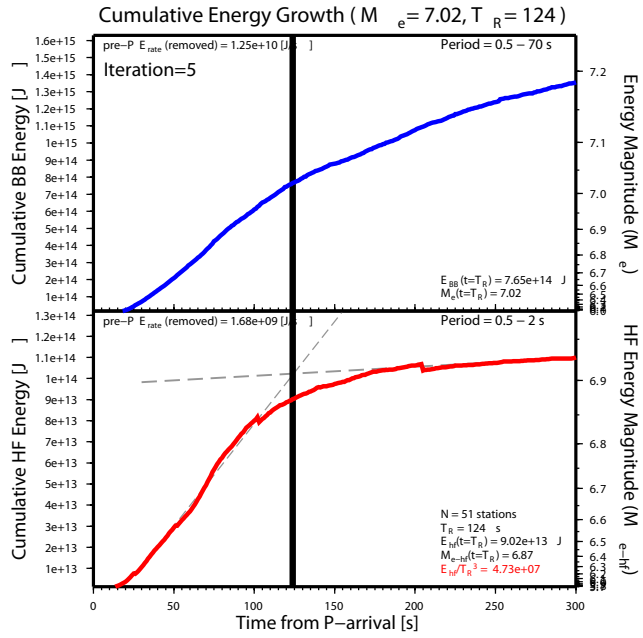
Cumulative Energy Growth (M e= 7.02, T R= 124)
Iteration=5
pre−P E rate (removed) = 1.25e+10 [J
Period = 0.5 − 70 s
E BB (t=T R) = 7.65e+14 J
M e(t=T R) = 7.02
pre−P E rate (removed) = 1.68e+09 [J
Period = 0.5 − 2 s
N = 51 stations
T R = 124 s
E hf(t=T R) = 9.02e+13 J
M e−hf(t=T R) = 6.87
E hf/T R 3 = 4.73e+07
Cumulative BB Energy [J]
Cumulative HF Energy [J]
Energy Magnitude (M e)
HF Energy Magnitude (M e−hf)
Time from P−arrival [s]

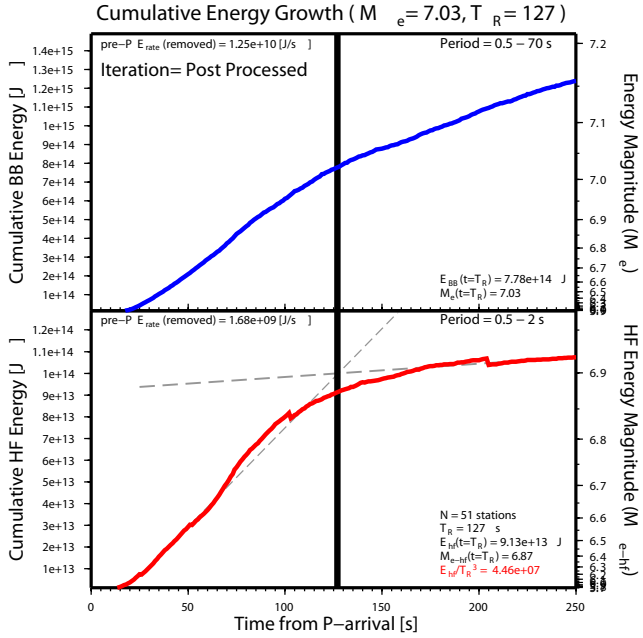
Cumulative Energy Growth (M e= 7.03, T R= 127)
Iteration= Post Processed
pre−P E rate (removed) = 1.25e+10 [J/s]
Period = 0.5 − 70 s
E BB (t=T R) = 7.78e+14 J
M e(t=T R) = 7.03
pre−P E rate (removed) = 1.68e+09 [J/s]
Period = 0.5 − 2 s
N = 51 stations
T R = 127 s
E hf(t=T R) = 9.13e+13 J
M e−hf(t=T R) = 6.87
E hf/T R 3 = 4.46e+07
Cumulative BB Energy [J]
Cumulative HF Energy [J]
Energy Magnitude (M e)
HF Energy Magnitude (M e−hf)
Time from P−arrival [s]

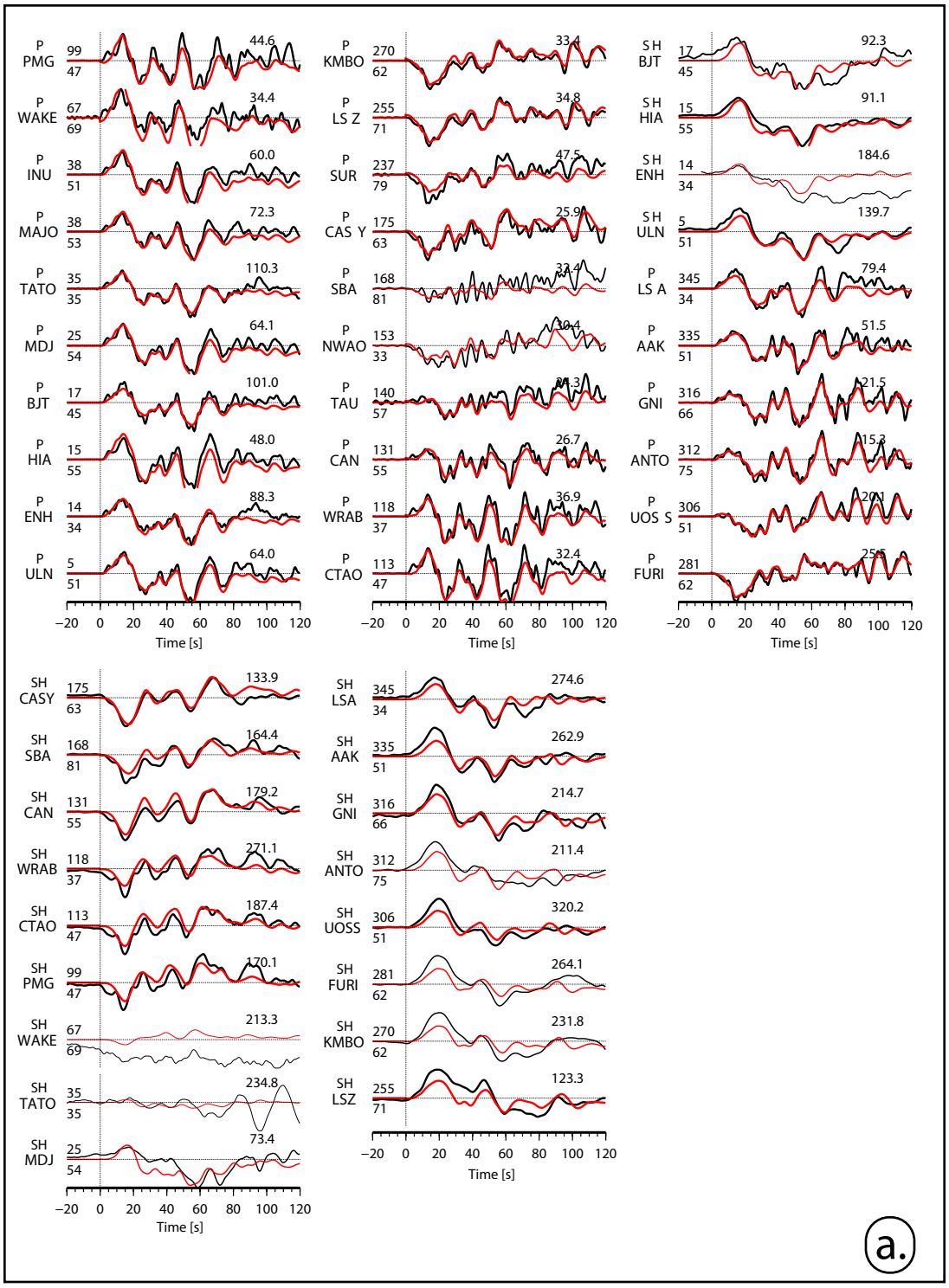
P PMG 99 47 44.6
P WAKE 67 69 34.4
P INU 38 51 60.0
P MAJO 38 53 72.3
P TATO 35 35 110.3
P MDJ 25 54 64.1
P BJT 17 45 101.0
P HIA 15 55 48.0
P ENH 14 34 88.3
P ULN 5 51 64.0
P KMBO 270 62 33.4
P LS Z 255 71 34.8
P SUR 237 79 47.5
P CAS Y 175 63 25.9
P SBA 168 81 32.4
P NWAO 153 33 30.4
P TAU 140 57 24.3
P CAN 131 55 26.7
P WRAB 118 37 36.9
P CTAO 113 47 32.4
SH BJT 17 45 92.3
SH HIA 15 55 91.1
SH ENH 14 34 184.6
SH ULN 5 51 139.7
P LS A 345 34 79.4
P AAK 335 51 51.5
P GNI 316 66 21.5
P ANTO 312 75 15.3
P UOS S 306 51 20.1
P FURI 281 62 25.5
SH CASY 175 63 133.9
SH SBA 168 81 164.4
SH CAN 131 55 179.2
SH WRAB 118 37 271.1
SH CTAO 113 47 187.4
SH PMG 99 47 170.1
SH WAKE 67 69 213.3
SH TATO 35 35 234.8
SH MDJ 25 54 73.4
SH LSA 345 34 274.6
SH AAK 335 51 262.9
SH GNI 316 66 214.7
SH ANTO 312 75 211.4
SH UOSS 306 51 320.2
SH FURI 281 62 264.1
SH KMBO 270 62 231.8
SH LSZ 255 71 123.3
−20 0 20 40 60 80 100 120
Time [s]
a.

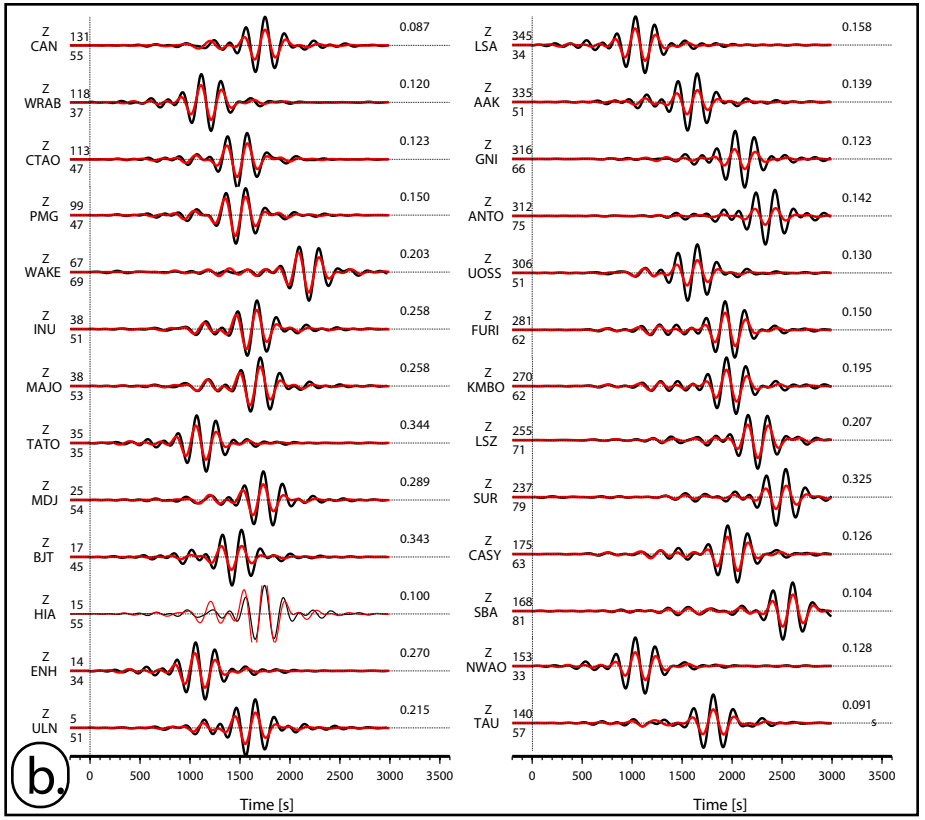
Z CAN 131 55 0.087
Z WRAB 118 37 0.120
Z CTAO 113 47 0.123
Z PMG 99 47 0.150
Z WAKE 67 69 0.203
Z INU 38 51 0.258
Z MAJO 38 53 0.258
Z TATO 35 35 0.344
Z MDJ 25 54 0.289
Z BJT 17 45 0.343
Z HIA 15 55 0.100
Z ENH 14 34 0.270
Z ULN 5 51 0.215
Z LSA 345 34 0.158
Z AAK 335 51 0.139
Z GNI 316 66 0.123
Z ANTO 312 75 0.142
Z UOSS 306 51 0.130
Z FURI 281 62 0.150
Z KMBO 270 62 0.195
Z LSZ 255 71 0.207
Z SUR 237 79 0.325
Z CASY 175 63 0.126
Z SBA 168 81 0.104
Z NWAO 153 33 0.128
Z TAU 140 57 0.091
0 500 1000 1500 2000 2500 3000 3500
Time [s]
b.

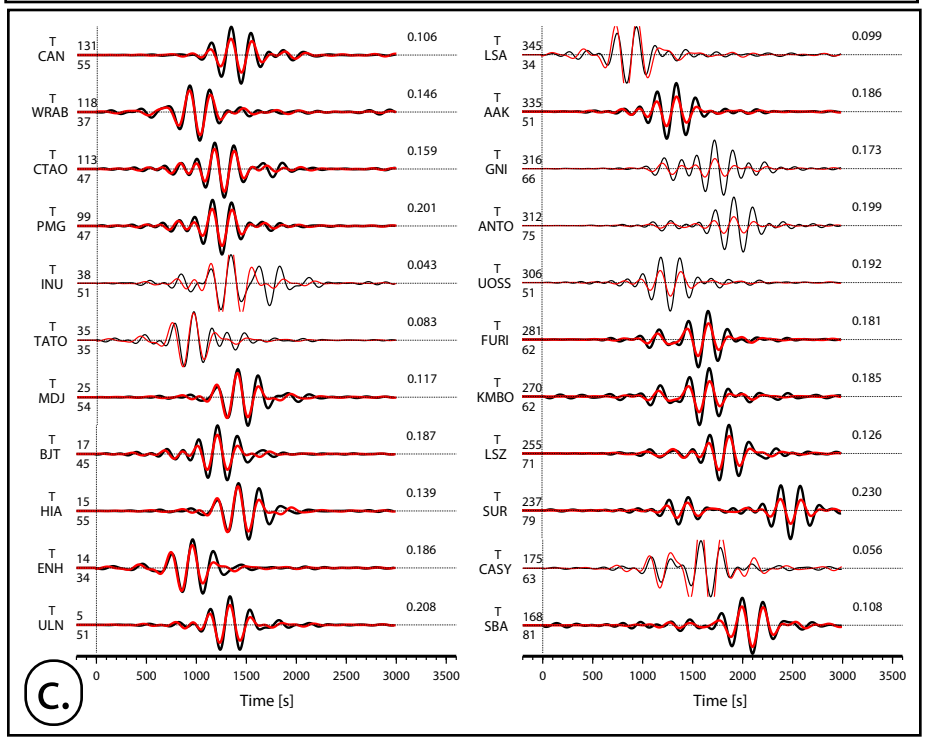
T CAN 131 55 0.106
T WRAB 118 37 0.146
T CTAO 113 47 0.159
T PMG 99 47 0.201
T INU 38 51 0.043
T TATO 35 35 0.083
T MDJ 25 54 0.117
T BJT 17 45 0.187
T HIA 15 55 0.139
T ENH 14 34 0.186
T ULN 5 51 0.208
T LSA 345 34 0.099
T AAK 335 51 0.186
T GNI 316 66 0.173
T ANTO 312 75 0.199
T UOSS 306 51 0.192
T FURI 281 62 0.181
T KMBO 270 62 0.185
T LSZ 255 71 0.126
T SUR 237 79 0.230
T CASY 175 63 0.056
T SBA 168 81 0.108
0 500 1000 1500 2000 2500 3000 3500
Time [s]
c.

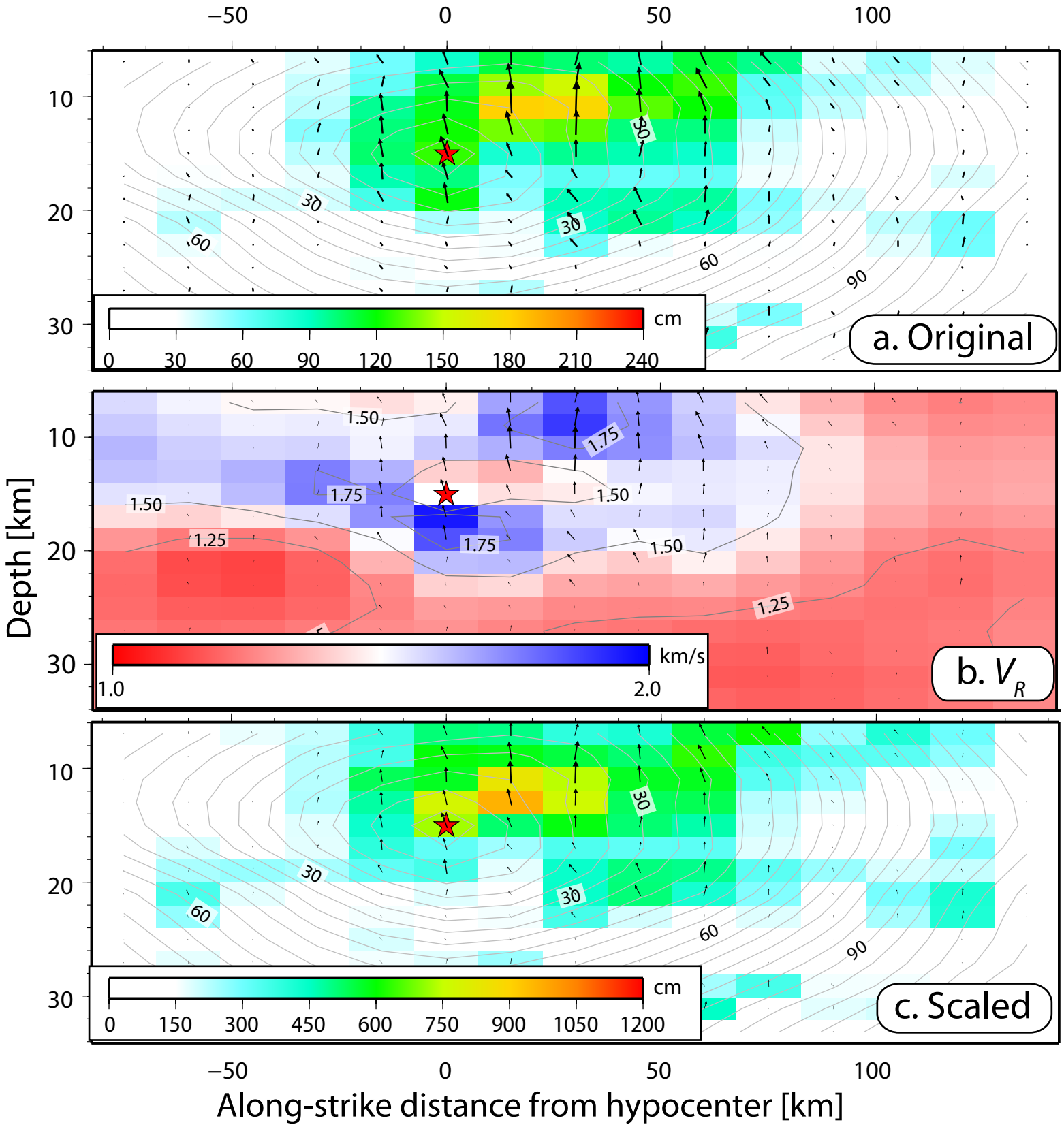
−50
0
50
100
10
20
30
Depth [km]
30
60
90
cm
0 30 60 90 120 150 180 210 240
a. Original
1.50
1.75
1.25
km/s
1.0
2.0
b. V_R
150 300 450 600 750 900 1050 1200
c. Scaled
Along-strike distance from hypocenter [km]

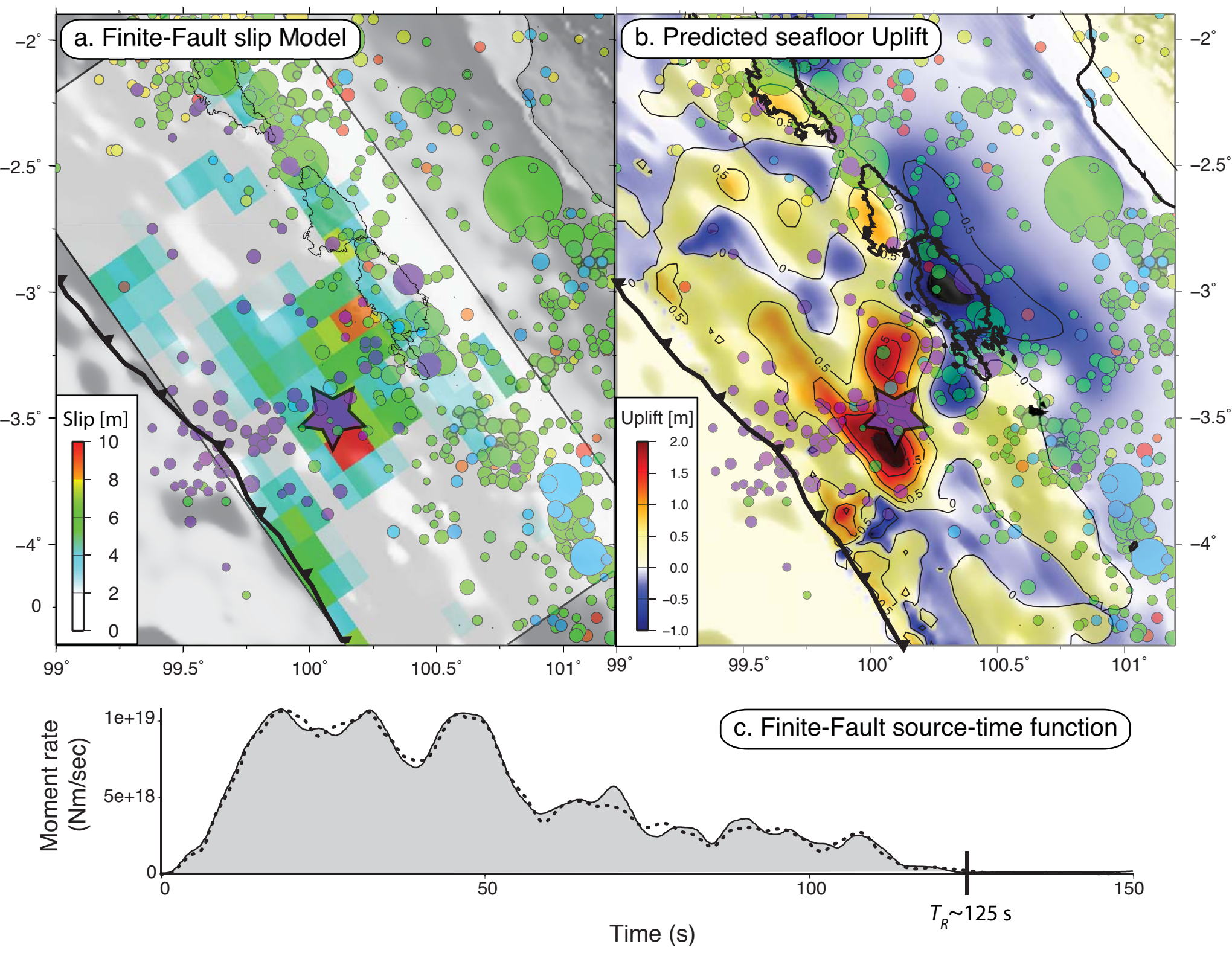
a. Finite-Fault slip Model
b. Predicted seafloor Uplift
Slip [m]
10
8
6
4
2
0
Uplift [m]
2.0
1.5
1.0
0.5
0.0
−0.5
−1.0
−2°
−2.5°
−3°
−3.5°
−4°
0
99°
99.5°
100°
100.5°
101°
c. Finite-Fault source-time function
Moment rate (Nm/sec)
1e+19
5e+18
0
0
50
100
150
T_R~125 s
Time (s)

Tsunami runup (m) in the west

12 9 6 3 0

(a)

-2.4
-2.6
-2.8
-3
-3.2
-3.4
100
100.5

Pulau Pagai-utara

Pulau Pagai-selatan

(b)

-1
-2
-3
-4
Mentawai Island
Sipura
Pagai-utara
Pagai-selatan
Indian Ocean
98 99 100 101

6 5 4 3 2 1 0

Max Amp. (m)

12 11 10 9 8 7 6 5 4 3 2 1 0

Tsunami runup (m) in the east

0 3 6 9 12

Wave Amp. (cm)

(c)

0
-10
~ 1600 km
56001
Indian Ocean
100 110

(d)

Buoy 56001

1
0
-1
1.5 2 2.5 3

Observation
Scaled model
Original model

TIme since earthquake (hour)